# Expanded Hydrated Vanadate for High-Performance Aqueous Zinc-ion Batteries

| | |
|---|---|
| Journal: | *Energy & Environmental Science* |
| Manuscript ID | EE-ART-03-2019-000956.R1 |
| Article Type: | Paper |
| Date Submitted by the Author: | 26-Apr-2019 |
| Complete List of Authors: | Liu, Chaofeng; University of Washington, Materials Science and Engineering<br>Neale, Zachary; University of Washington<br>Zheng, Jiqi; University of Washington<br>Jia, Xiaoxiao; University of Washington<br>Huang, Juanjuan; University of Washington<br>Yan, Mengyu; Wuhan University of Technology, State Key Laboratory of Advanced Technology for Materials Synthesis and Processing; University of Washington,  Material Science and engineering<br>Tian, Meng; University of Washington<br>Wang, Ming-Shan; University of Washington, Materials Science and Engineering<br>Yang, Jihui; University of Washington, Materials Science and Engineering<br>Cao, Guozhong; University of Washington, Materials Science and Engineering |
| | |

# Expanded Hydrated Vanadate for High-Performance Aqueous Zinc-ion Batteries

Chaofeng Liu, Zachary Neale, Jiqi Zheng, Xiaoxiao Jia, Juanjuan Huang, Mengyu Yan, Meng Tian, Mingshan Wang, Jihui Yang*, Guozhong Cao*

Department of Materials Science and Engineering, University of Washington, WA

Corresponding authors: J. Yang (jihuiy@uw.edu) and G.Z. Cao (gzcao@uw.edu)

## Abstract

Hydrated vanadates are promising layered cathodes for aqueous zinc-ion batteries owing to their specific capacity as high as 400 mAh/g; however, the structural instability causes a serious cycling degradation through repeated intercalation/deintercalation reaction. This study reveals the chemically inserted Mn (II) cations act as structural pillars, expand the interplanar spacing, connect the adjacent layers as well as partially reduce pentavalent vanadium cations to tetravalent. The expanded interplanar spacing to 12.9 Å, reduces electrostatic interaction, and transition metal cations collectively promote and catalyze fast and more zinc ion intercalation at higher discharge current densities with much enhanced reversibility and cycling stability. Manganese expanded hydrated vanadate (MnVO) delivers a specific capacity of 415 mAh/g at a current density of 50 mA/g and 260 mAh/g at 4 A/g with capacity retention of 92% over 2,000 cycles. The energy efficiency increases from 41% for hydrated vanadium pentoxide (VOH) to 70% for MnVO at 4 A/g and the open circuit voltage maintains at 85% of the cutoff voltage in the MnVO battery on the shelf after 50 days. Expanding hydrated vanadate with other transition metal cations for high-performance aqueous zinc-ion batteries are also obtained, suggesting it is a general strategy for exploiting the high-performances cathodes for multi-valent ion batteries.

Keywords: Hydrated vanadate, Layered cathode, Manganese cation, Zinc ion battery

## Introduction

Layered materials offering sufficient intercalating channels and active sites for working cations transportation and accommodation have become the most competitive electrode materials for supporting commercial applications of the rechargeable batteries,[1-7] especially the secondary Li ion batteries based on lithium cobalt oxide and graphite which have brought a revolution to portable electronics and communication.[8-11] However, the layered cathodes in the flammable and highly volatile nonaqueous electrolytes introduce serious safety issues when oxygen released from the layered cathode penetrates to the anode causing thermal runaways.[12] Aqueous electrolytes endow the rechargeable batteries improved safe protection, but the limited voltage window and single-electron carriers seriously restrain the energy density of batteries, even if high concentration salt solutions and "water-in-salt" electrolytes were introduced in Li-ion systems.[13, 14] Multivalent ions such as $Mg^{2+}$,[15] $Zn^{2+}$,[16] $Ca^{2+}$ [17]and $Al^{3+}$ [18] carry more charges per ion than $Li^{+}$ or $Na^{+}$ and are believed as promising working ions in rechargeable batteries. Among all multivalent ions mentioned above, $Zn^{2+}$ has a smaller ionic radius of 0.74 Å in a six-fold coordination and Zn metal anode has a high volumetric capacity around 5850 $mAh/cm^{-3}$,thus aqueous zinc ion batteries (AZIBs) have been becoming a hot research field.[16, 19-21] Before any new breakthrough happens in the present voltage-limited aqueous electrolytes, exploiting cathodes with high specific capacity is an effective way to achieve an increase in battery energy density.

Cathode materials for ZAIBs mainly include manganese oxides,[22-28] vanadium oxides,[29-36] Prussian blue and its analogues,[37-40] transition metal dichalcogenides[41-44] and organic compounds.[45, 46] Manganese dioxides can be classified into one-, two- and three-dimensional tunnel structures that influence their electrochemical activities for Zn ion storage.[16, 19] The partially irreversible phase transition and the dissolution of active materials cause an unstable cycling performance.[21, 24, 47] Prussian blue, the mixed-valence hexacyanoferrates with an open framework, has a tunable lattice spacing through introducing different transition metal cations,[38, 48] but the lower specific capacity of < 100 mAh/g makes them uncompetitive in comparison with manganese oxides of 300 mAh/g.[16, 19] Dichalcogenides deliver a considerable specific capacity around 200 mAh/g, however, the intrinsically low electrical conductivity and discharge voltage restrain their energy density and efficiency.[44, 49] Although organic compounds present a promising Zn ion storage capability, the dissolvable species formed in the cycling process cause a rapid capacity fading.[45] Layered vanadate compounds as one of the cathode categories for Zn-ion batteries can deliver a specific capacity as high as 400 mAh/g owing to the variable chemical valence of vanadium ion from 5+ to 3+ and its tunable interlayer distance for Zn-ion access and diffusion.[16, 21] Additionally, vanadium element has a considerable abundance of 190 ppm in the Earth's crust, leading to a lower cost than that of cobalt widely used in commercial Li-ion batteries.[50] Layered vanadium pentoxide, a common cathode for Li- and Na-ion batteries, in aqueous Zn ion batteries delivered an increasing cycling gravimetric capacity due to the exfoliation of the initial chunks to allow more reactive sites.[30] Hydrated vanadium pentoxide ($V_2O_5 \cdot nH_2O$, VOH) has a bilayer structure and structural water molecules work as the pillar to expand the layer spacing to near 12 Å. More importantly, the shielding effect from water decreases the interaction between cations and plays a role to accelerate Zn ion diffusion.[51] In order to improve the reaction kinetics of VOH, an essential strategy is to introduce some alien cations into the interlayers to enlarge the spacing. It was found that the bigger radius of the alien cations could produce a larger layer distance and obtain a faster ion diffusion. For example, hydrated $Mg^{2+}$ with a radius of 4.3 Å creates an interlayer spacing of 13.4 Å in VOH, which is larger than 11.07 Å in hydrated $Li^+$ expanded VOH because hydrated $Li^+$ has a smaller radius of 3.8 Å.[52, 53] Similar studies have also been done with preinserted calcium and zinc cations.[36, 54] However, the introduced cations just play a role in expanding the lattice spacing to accelerate the ion diffusion, the electrochemical stability of host materials still suffer from structural degradation, especially with the possibility that alien cations deintercalate during the cycling processes because of the weak Van der Waals interaction between hydrated alien cations and oxygens from layered slabs of the host. Compared with the weak interactions, the ideal situation is chemical bonding to lock the layered slabs and endow the host material a stable cycling stability for intercalation/deintercalation reactions without sacrificing the interplanar spacing.

In this paper, Mn (II) cation expanded hydrated vanadium pentoxide (MnVO) is prepared through a hydrothermal method and shows much larger storage capacity and higher discharge voltage, and enhanced rate capability and cycling stability in comparison with VOH owing collectively to enlarged interplanar spacing, stabilizing effect from Mn (II) pillars, catalytic effect, and improved charge and ion transport properties. The increased energy efficiency and reduced voltage degradation reveal a great potentiality for commercial applications. More importantly, other transition metal cations (TMCs), such as Co and Ni, are also introduced and present the same structures and functionalities to enhance the Zn-ion storage performance in an aqueous system, implying introducing TMCs is an effective and general strategy for improving the layered VOH cathode.

## Experimental

All chemicals were used as received without purification. 2 mmol of $V_2O_5$ (99.6+%, Sigma-Aldrich) was dissolved into 50 mL of DI $H_2O$ with 2 mL of $H_2O_2$ (30%, Fisher chemical), and 1 mmol of $MnSO_4 \cdot 10H_2O$ (98.3%, Fisher scientific) was dissolved separately into 30 mL of DI water. Two solutions were admixed and transferred to a 100 mL (internal diameter of 42 mm with a height of 72 mm) Teflon lined stainless steel autoclave and heated to and held at 120 ˚C for 6 h. Brick red precipitates were collected by centrifugation and washed by water and ethanol for three times. The collected precipitates were dried at 70 ˚C overnight in an electric oven and turned greenish. The resulting product (MnVO) was further dried at 120 ˚C in a vacuum oven. VOH was synthesized with the same procedure and processing conditions without Mn (II) sources, 80 mL of DI water was used in order to attain the same internal reactive pressure in the Teflon bottle and the resulting product was dried by a freezing dryer at -52 ˚C. For Co (II) and Ni (II) stabilized samples, their sulfate salts were used to synthesize the desired samples and the processes were identical to the MnVO synthesis.

Phase identification was carried out by a Bruker X-ray diffractometer (D8 Discover with IμS 2-D detection system) at an accelerating voltage of 50 kV and a working current of 1000 μA. A Fourier Transform Infrared Spectrometer (FT-IR, Bruker, VERTEX 70) was used to collect the functional groups' stretching or bending information from 400 to 4500 $cm^{-1}$ and a Renishaw InVia Raman Microscope equipped with the Leica DMIRBE inverted optical microscope was also used to obtain the chemical bond information by one of the laser excitation sources at 514 nm. A differential scanning calorimeter (DSC 3+ STAR$^e$ System, Mettler Toledo) was adopted to analyze the thermal stability of sample within 40-700 ˚C in a flowing nitrogen gas (50 sccm). The microstructures of samples were observed by a scanning electron microscope (SEM, FEI Sirion) at a working voltage of 5 kV and a scanning transmission electron microscope (S/TEM, Tecnai G2 F20) with an accelerating voltage of 200 kV. The surface chemical states of samples were determined using a Kratos Axis Ultra DLD X-ray Photoelectron Spectroscopy system (XPS) with an Al$K\alpha$ radiation source that was operated at 10 mA and 15 kV, and with a charge neutralizer. The angle between the specimen normal and the spectrometer was 0˚.

For the electrode preparation, the active material was mixed with conductive carbon and polyvinylidene fluoride (PVDF) binder in a weight ratio of 7:2:1 in N-Methyl-2-Pyrrolidone (NMP) solvent to obtain a slurry that was pasted on a current collector - titanium foil. The prepared electrodes were dried in a vacuum oven at 120 ˚C overnight. The mass loading of active materials is 3 - 4 mg/$cm^2$. Zn metal was used as the anode and 80 μL of 3 M zinc trifluoromethanesulfonate (98%, $Zn(CF_3SO_3)_2$) aqueous solution was injected into the batteries as the electrolyte. A glass fiber filter (Whatman, Grade GF/A) was used as the separator. The redox characteristics of cathodes were tested by cyclic voltammogram (CV) on a Solartron electrochemical station (SI 1287) equipped with an electrochemical impedance spectroscopy system (EIS, SI 1260). Galvanostatic intermittent titration technique (GITT) was applied to analyze the reaction and diffusion kinetics at a current density of 50 mA/g and the charging/discharging time and interval of 10 min for each step. The Galvanostatic charge and discharge tests were conducted by a Neware tester (CT-4008).

The working voltage of cells was set from 0.2 to 1.6 V versus $Zn^{2+}/Zn$, and the EIS measurements have a frequency range between $10^5$ and 0.01 Hz.

## Results and Discussion

Figure 1a compares the XRD patterns of MnVO and VOH, in which VOH is well indexed with the standard peaks ($V_2O_5{\cdot}nH_2O$, PDF 40-1296) and MnVO shows the same diffraction peaks as reported $M_xV_2O_5A_y{\cdot}nH_2O$ (M= cations, A= anions)[55]. However, the Miller indices corresponding to crystallographic planes does not exist in the current database. The structure of $M_xV_2O_5A_y{\cdot}nH_2O$ is believed to consist of stacked V-O double layers and the adjacent layers are separated by water and cations and anions added in the preparation.[55] The strongest peak at 6.8° in MnVO corresponds to a larger lattice spacing of 12.9 Å and VOH has the strongest peak at 7.4° with a lattice spacing of 11.9 Å that agrees with the reported ~11.5 Å,[56] suggesting the introduction of Mn (II) with water together can expand the interlayer spacing further as reported in Mg preinserted VOH.[52] In the FTIR spectra (Figure 1b), peaks at 461 and 737 $cm^{-1}$ originates from the symmetric stretching vibration of the O-V-O bonds and the peak located at 992 $cm^{-1}$ is attributed to the stretching vibration of the V=O bonds.[57] The bending and stretching vibration of O-H from structural water appears around 1612 and 3450 $cm^{-1}$,[58] respectively. Upon careful examination, a slight red-shift (2-5 $cm^{-1}$) of V-O vibrations appears in MnVO in comparison with VOH, suggesting the V-O bond becomes weak because a fraction of $V^{5+}$ is reduced to $V^{4+}$ in MnVO,[59] the details on chemical states will be discussed further with the XPS results. The similarity in FT-IR spectra reveals similar crystal structures in both samples. Raman spectra (Figure 1c), as the complementary fingerprints of samples to the FT-IR spectra, were collected. The peak located at 159 $cm^{-1}$ comes from the bending vibration of the -O-V-O-V- chains, which implies an *a*-directional compressive deformation in the lattice.[60] A blue shift of 4 $cm^{-1}$ in MnVO verifies the stronger compression along the *a*- direction due to the possible electrostatic interaction between Mn(II) and O. The bending vibration of the V=O bond formed by terminal O and center V cation appears at 264 $cm^{-1}$,[61] and the red shift of 4 $cm^{-1}$ in MnVO means the elongation of V=O along the *c*- direction, consistent with the XRD results of the lowest angle. The board peak around 352 $cm^{-1}$ is related to the librational motions of water.[62] The triply coordinated $O_3$ by three V cations forms a $V_3$-O bond that connects three edge sharing $VO_5$ pyramids in the crystal structure[56] and is reflected by a stretching signal at 512 $cm^{-1}$ [61] and a red shift of 5 $cm^{-1}$ in MnVO suggests a lattice expansion along the *b*- direction. The bridging O links two corner-sharing $VO_5$ polyhedra and stretching vibration of $V_2$-O appears at 706 $cm^{-1}$,[61, 63] and the peak at 674 $cm^{-1}$ from stretching of $V_2$-O suggests a partially disordered V-O-V connection existed in the host lattice.[63] The weakened peak at 674 $cm^{-1}$ in MnVO reveal a better crystallinity and the possible reason is that the introduced Mn (II) makes the arrangement of V and O to be more orderly because the interaction among the three ionic species. The peak at 891 $cm^{-1}$ is attributed to the stretching of V-$OH_2$.[64] A weakened V-$OH_2$ bond appears in MnVO because of the red shift, which implies water have more rotational freedom in the interlayer.[62] The competing interaction from Mn(II) and water could influence the bond strength of V-$OH_2$. Compared the spectra of 600-800 $cm^{-1}$ of both samples, a broad peak appears at 674 $cm^{-1}$ in MnVO rather than the sharp peak in VOH. Lorentz functions were used to obtain the details of chemical bonds, two discernable peaks at 674 and 706 $cm^{-1}$ fit well with the stretching of $V_2$-O in VOH (Figure 1d), and a weak peak at 652 $cm^{-1}$ corresponds to the vibration of Mn-O bond in $MnO_6$ octahedra of MnVO (Figure 1e),[65] suggesting Mn (II) ions connect [$VO_n$] layers by chemical bonds. It should be mentioned that the bending or stretching signal of sulfate anion is not detected in Raman or FT-IR spectra, demonstrating no sulfate anion in MnVO. Based on the structural comparison, it can be speculated that MnVO has two possible structures. One is the bi-layer structure in which Mn (II) cations reside into the interlayers like a slight structure distortion in VOH, it can be called by a pre-inserted cation as sodium in $V_2O_5$.[66] The other is to form a new phase as $MnV_{12}O_{31}\cdot 10H_2O$ (PDF 47-0146)[67] which has the same XRD pattern as $M_xV_2O_5A_y\cdot nH_2O$ but no crystal structure details can be found in the current database. For the former, preinserted cations, such as $Li^{+}$[53] and $Mg^{2+}$,[52] in VOH seldom cause a big difference in the XRD patterns. The changes in the XRD pattern means the formation of new phases, but the analysis based on the FT-IR and Raman spectra demonstrate both samples have the similar chemical bonds. Combining the structural information discussed above, MnVO is likely to have a similar crystal structure as VOH and the preinserted Mn (II) in the interlayer forms the chemical bonds.

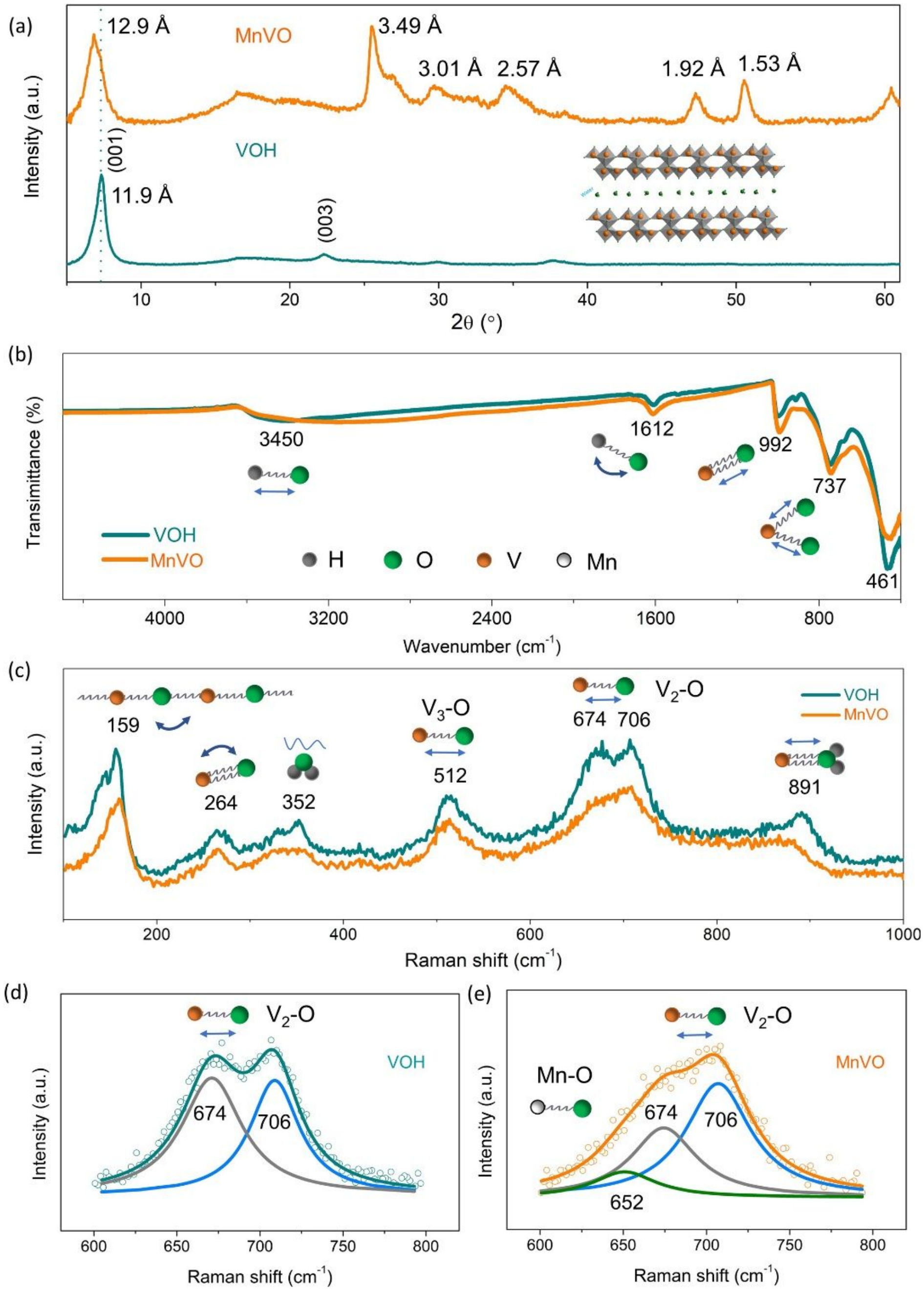

Figure 1. (a) XRD patterns of MnVO and VOH. (b) FT-IR and (c) Raman spectra of MnVO and VOH, the vibrations from V-O, O-H, and water are detected. The similarity of both spectra demonstrated MnVO has the similar structure as VOH. However, the changed chemical bonds indicate the introduced Mn (II) likely sit into the interlayers. The partially fitted Raman spectra of (d) VOH and (e) MnVO. The peak at 652 $cm^{-1}$ corresponded to Mn-O in $MnO_6$ octahedra demonstrates a chemical connection formed between Mn (II) and O.

Figure 2a shows TEM images in which MnVO consists of nanosheets. The nanosheets aggregate to form a micro-flower-like shape as observed by SEM (Figure S1). EDS mapping collected by TEM exhibits homogeneous element distributions of Mn, V and O in the resulting MnVO sample, and the lattice spacing of 12.9 Å is in accordance with the XRD results. No sulfur was detected, which supports the argument about no anion ($SO_4^{2-}$) in MnVO interlayers as mentioned in the structural analysis. To confirm the effects of Mn (II) on the structural stability, DSC/TGA is used to analyze the water loss and possible phase transition in the heating process. Water loss in both samples (Figure 2b) accompanied with a continuous endothermal process is reflected by two weak peaks at 150 and 380 ˚C and the endothermal peak appearing around 685 ˚C is attributed to the melting of $V_2O_5$.[68] It is worth noting that the end temperature for water loss from MnVO (475 ˚C) is higher than that from VOH (380 ˚C) as marked by the dotted lines, suggesting water has a better structural stability derived from the interaction by Mn in MnVO. The water content in MnVO (15 *wt*%) is less than that in VOH (17 *wt*%). The introduction of Mn (II) could induce a change in chemical valence of $V^{5+}$ because of the electroneutrality required in the lattice. Survey XPS spectra (Figure S2) compare the characteristic peaks and Mn2p signal is only detected in MnVO, which agrees with the elements in the XRD detected phase. No signal relating to S is detected in either samples, demonstrating no sulfate anion in MnVO and the structure speculation is reasonable. Characteristic peaks at 517.4 and 517.0 eV in the XPS spectrum of $V2p_{3/2}$ (Figure 2c) are originated from $V^{5+}$, the difference of binding energy means the local chemical surroundings are different for some $V^{5+}$, in particular Mn (II) at 642.2 eV (Figure 2d) and $V^{4+}$ at 516.4 eV were also detected in literature.[69] The detected divalent state of Mn cation verifies no oxidizing reaction happens on Mn (II) in the synthesis processes. The ratio of $V^{4+}$ in MnVO and VOH are 18.9% and 13.2% (Figure S3 and 2c), respectively, determined by evaluating the integrated area in the fitting spectra. The appearance of $V^{4+}$ in VOH is possibly from a reduction reaction between $V_2O_5$ and $H_2O_2$ to form $VO(O_2)^+$ in the synthesis process.[70] More $V^{4+}$ detected in MnVO is attributed to the introduced Mn (II) and the appearance of $V^{4+}$ implies oxygen vacancies in VOH and MnVO as reported in $V_2O_5$ or VOH.[71, 72] The impacts from oxygen vacancies are close in both samples because the similar amounts of $V^{4+}$, thus the differences on electrochemical performances derives from the introduced Mn (II). V$^{4+}$ has a bigger ionic radius of 72 pm than that of 68 pm for V$^{5+}$ in a six coordination, which further expands the lattice spacing. At the same time, Mn (II) and V$^{4+}$ have electrons in their 3*d* orbital beneficial for enhancing the electrical conductivity and catalyzing the electrochemical reaction; when Mn (II) cations and oxygen vacancies are introduced, the number of *d* orbitals located at the bottom of the conduction band and the upper of the valence band increases.[72, 73] Both samples have a similar surface area of 50 m$^2$/g (Figure S4), and it is unlikely that their surface area would make significantly different influences on the electrochemical performances.

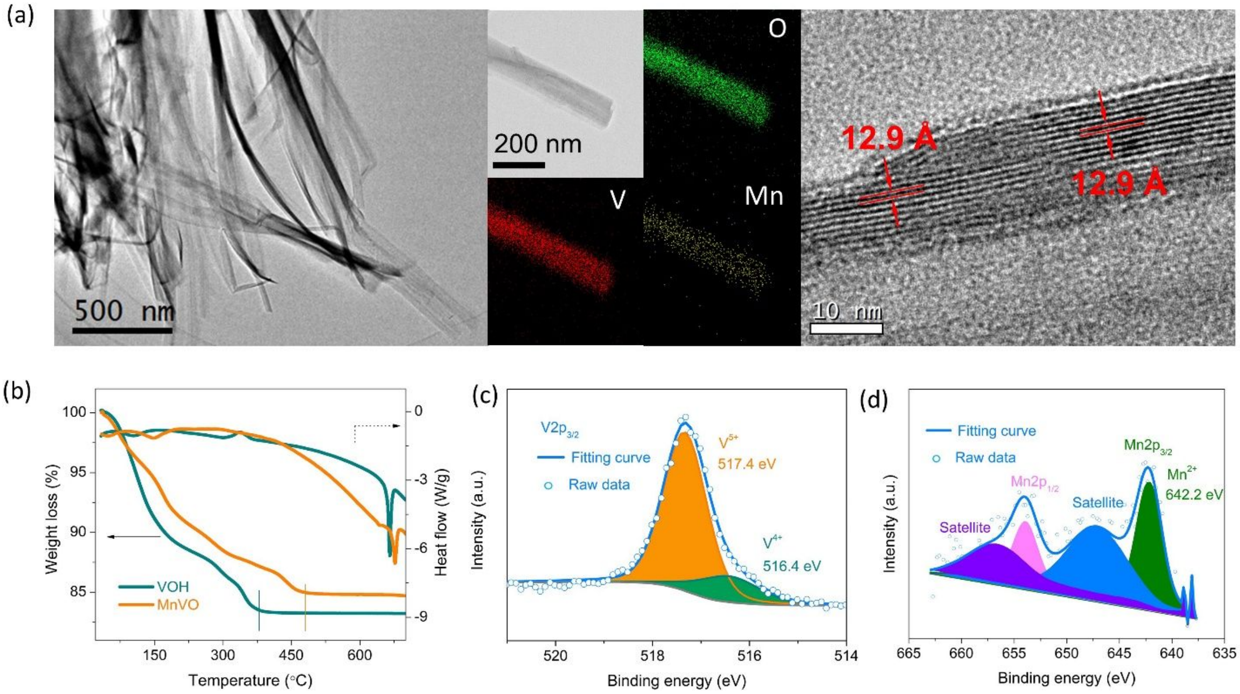

Figure 2. (a) TEM with EDS mapping and high resolution TEM image of MnVO. The thin nanosheet have homogeneous element distribution and the discernable lattice spacing of 12.9 Å agrees with the XRD data. (b) Differential scanning calorimetry curves from MnVO and VOH, the downward endothermal curve of MnVO suggests MnVO having a more stable crystal water. (c) XPS spectrum of V2p$_{3/2}$ of MnVO and tetravalent vanadium cation was detected and the amount is around 18.9 % by calculated the area ratio of the fitting spectra. (d) XPS spectrum of MnVO collected from divalent Mn that demonstrates no redox reaction happened on Mn (II) ion in the synthesis processes.

Redox reaction in MnVO was analyzed by the CV test and two pairs of peaks are shown in Figure 3a, the peak pair resided at higher voltage (1 V) is related to redox pair of $V^{5+}/V^{4+}$ and the transition of $V^{4+}/V^{3+}$ pair appears around 0.5 V.[51, 74, 75] The overlapped CV curves in the first three cycles mean a reversible reaction of MnVO cathode in the aqueous Zn-ion battery. An interesting phenomenon is that the first discharge peak around 1 V shifts to a higher voltage in the subsequent cycles, possibly attributed to the local chemical surroundings change after Zn ion insertion. However, VOH has deviating peaks in the first three cycles and the discharge peaks shifts to lower voltage upon cycling (Figure S5.) Figure 3b compares the CV curves of both cathodes collected at 0.1 mV/s and smaller voltage differentiations in redox pairs of MnVO as listed in Table 1, meaning MnVO cathode has a smaller polarization and better reactive kinetics in the electrochemical processes. To analyze the reaction kinetics, various sweeping rates of CV curves were collected as shown in Figure 3c and cathodic peaks shift toward higher voltages and anodic peaks move back to lower voltages with the increasing sweeping rates owing to the polarizations,[46] especially phase transition happening in the electrode.[32] Peak currents ($i$) and sweep rates ($v$) obey a power-law relationship that is described by

$$i = a\, v^{b} \quad , \tag{1}$$

where $a$ and $b$ are variables. $b$ value of 1 indicates surface capacitance dominated charge storage and 0.5 is indicative of a mass diffusion-controlled charge storage.[76-78] The $b$ values of peaks a-d in MnVO are 0.65, 0.86, 0.81 and 0.84 (Figure 3d), whereas the values of peaks a'-d' from VOH are 0.65, 0.76, 0.81 and 0.73 (Figure S6). These suggest both samples have the considerable kinetics and the electrochemical reactions are limited by ion diffusion and capacitor-like behavior partially contributes to the charge storage.

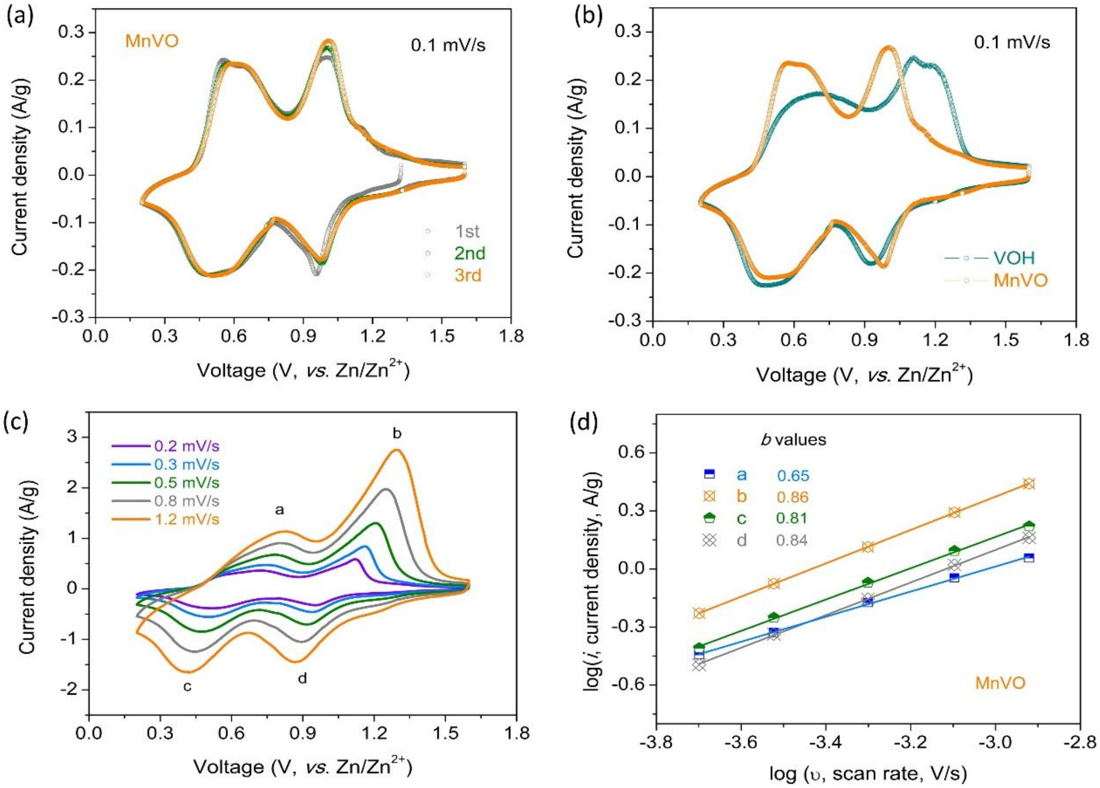

Figure 3. (a) CV curves of MnVO collected at a sweep rate of 0.1 mV/s. The overlapping of the curves in the first three cycles means a good reactive reversibility in MnVO. (b) Comparison of CV curves of MnVO and VOH. The smaller voltage deviation in the redox pairs of MnVO suggests a better reaction kinetics and reversibility. (c) CV curves of MnVO at various sweep rates and (d) the relationship between peak currents and sweep rates.

Table 1. The redox pairs and voltage differentiation in both cathode materials

| Samples ID | Redox pairs (V) | Differentiation (V) |
|---|---|---|
| VOH | 1.15/0.93 | 0.23 |
| | 0.69/0.48 | 0.11 |
| MnVO | 1.01/0.98 | 0.03 |
| | 0.61/0.52 | 0.09 |

Voltage profiles of MnVO is shown in Figure 4a and the delivered specific capacity is 415 mAh/g at a current density of 50 mA/g, which is higher than that of other vanadium-based cathodes, such as Li intercalated $V_2O_5{\cdot}nH_2O$,[53] $Na_2V_6O_{16}{\cdot}3H_2O$,[34] $H_2V_3O_8$,[79] $VO_2$,[32, 75] $LiV_3O_8$,[80] or

$Mg_xV_2O_5{\cdot}nH_2O$.[52] The sloping curves agree with the board redox peaks in CV test, and the increased voltage and overlapped curves in the subsequent cycles suggests the highly reactive reversibility. In the rate capability tests (Figure 4b), MnVO electrode with a mass loading of 3-4 $mg/cm^2$ delivers an initial specific capacity of 380 mAh/g at a current density of 0.5 A/g, and VOH has a capacity of 287 mAh/g. The difference is that VOH presents a capacity increase to 326 mAh/g after the first five cycles, but MnVO displays a relatively stable capacity at 371 mAh/g. With current density increasing from 1, 2, 4 to 8 A/g, MnVO delivers the specific capacities of 347, 310, 268 and 214 mAh/g, respectively, and VOH exhibits the capacities of 280, 237, 179 and 124 mAh/g at the corresponding conditions. The capacity retention in MnVO is 56 % that is higher than that of 38% in VOH at 8 A/g compared with their capacities at 0.5 A/g, it is also more superior in comparison with $VO_2$ [74] and $Mg_xV_2O_5{\cdot}nH_2O$ [52] (Table S1). When the current densities decrease back to 0.5 A/g from 8 A/g, the capacities recover to the initial values, suggesting a stable crystal structure and great electrochemical reversibility. During the high current cycling tests (Figure 4c), MnVO presents excellent stability after a slight capacity increase owing to the electrolyte penetration and electrochemical activation in the first several cycles.[52] The stable specific capacity is around 260 mAh/g that closes to the result from rate test at the same current density of 4 A/g. However, the specific capacity of VOH decreases rapidly and capacity retention is 66% over 500 cycles, which is lower than 96% capacity retention over 2,000 cycles in MnVO. The capacity retention of MnVO is also higher than that of $Zn_{0.25}V_2O_5{\cdot}nH_2O$ (80% over 1,000 at 2.4 A/g)[36] and $LiV_2(PO_4)_3$ cathode (~75% over 4,000 cycles at 1.5 A/g).[81] The maximum energy and power densities of MnVOH are 267 Wh/kg and 5,791 W/kg, respectively, which are higher than 224 Wh/kg and 4,244 W/kg of VOH as shown in Ragone plot (Figure S7). Voltage hysteresis collected at 4 A/g exhibit the remarkable differences between the two, but this essential indicator for evaluating the practical possibility is ignored in the current reports on zinc ion batteries. As shown in Figure 4d, MnVO, at the initial cycle(s), delivers a higher specific capacity of 251 mA/g with a mid-value voltage of 0.61 V, which are higher than the specific capacity of 216 mAh/g and 0.47 V in VOH. At the 50th cycles, the specific capacity of MnVO has a slight increase to 275 mAh/g and an increased mid-value voltage of 0.67 V. However, VOH presents a decrease on specific capacity to 92 mAh/g with a slight increased mid-value voltage of 0.51 V. More importantly, energy efficiency (EE), defined by the ratio of discharge and charge energy densities in a battery performance to evaluate the practicability,[82] is 70% calculated in the 50th cycle of MnVO and its initial EE is 59%. The hysteresis area encompassed by the charging and discharging curves in Figure 4e reflects the energy loss in one cycle. The larger area means lower EE and higher energy loss in the battery. For VOH, it has an initial EE of 40% (Figure S8) and maintains at 41% in the 50th cycle, meaning an energy loss reaches up to ~60%. Voltage degradations (Figure 4f) on the shelf, another practical parameter to evaluate batteries' self-discharge,[83] were also monitored after the fully charging process at a current density of 50 mA/g. Open circuit voltage of MnVO battery maintains at 1.36 V (85% of the cutoff voltage) after 50 days, but VOH degrades to 1.29 V, suggesting a less self-discharge reaction happens in MnVO. Generally, the voltage degradation on the shelf comes from the charge redistribution and reverse ion transport between two electrodes.[84] The better electrochemical performances in MnVO can be attributed to the introduced Mn (II) that combined with water to expand the interlayer spacing for benefiting the ion diffusion to enhance the rate capability and decrease the polarizations at a high current density. Mn (II) cation carries positive charge that would form chemical interaction with terminal oxygen from [$VO_n$] layers to stabilize the crystal structure, which guarantees the structural stability under the fast Zn ion insertion and extraction and decrease the ion self-diffusion to restrain the degradation on open circuit voltage when batteries are on the shelf with a long time. In addition, more $V^{4+}$ induced by Mn (II) has a positive effect for the improved electrochemical performance owing its larger ionic radius and one electron in the 3*d* orbital, which lead to a more expanded lattice spacing and enhanced electrical conductivity to catalyze the phase transition.

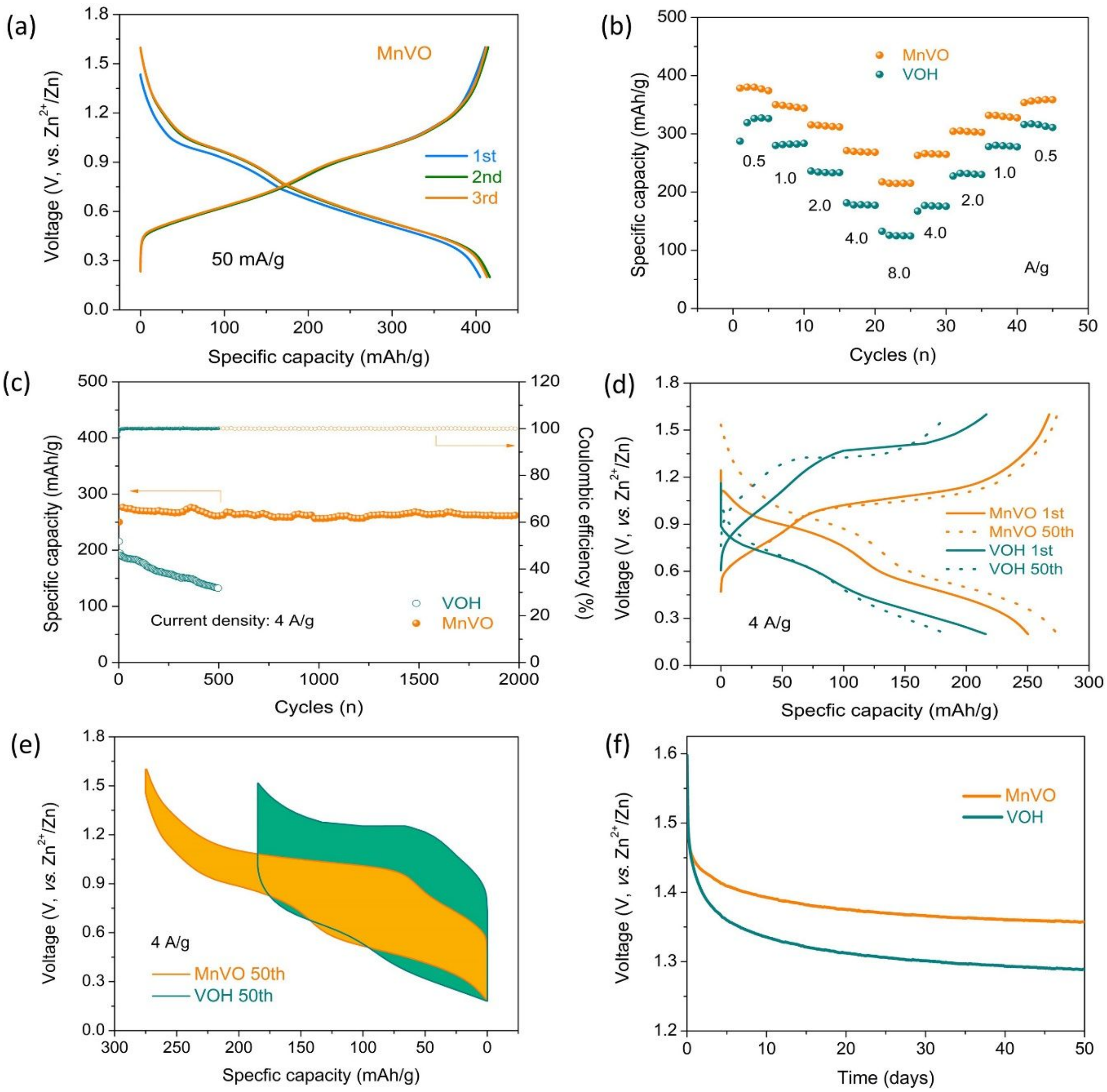

Figure 4. (a) Voltage profiles of MnVO at 50 mA/g. (b) Rate capability and (c) Cycling stability of both cathodes in the aqueous Zn-ion battery. (d) Voltage profiles at the 1st and 50th cycles collected at 4 A/g, the smaller polarization and higher energy efficiency in MnVO suggest the introduced Mn (II) cation benefits ion diffusion and stabilizes the crystal structures under fast ion insertion and extraction. (e) Voltage hysteresis of MnVO and VOH collected at 4 A/g in the 50th cycle. The area encompassed by charging and discharging curves is the energy loss in the cycle, MnVO display a smaller energy loss and higher energy efficiency. (f) Open circuit voltage degradations of batteries on the shelf. The less voltage loss means the weak self-discharge and the stable electrochemical performance.

To confirm the charge storage mechanism, the phase transitions in the electrochemical processes were detected by *ex-situ* XRD and the patterns are shown in Figure 5a. The pristine electrode was fully discharged to 0.2 V, the strongest peak at 6.8° moves to a lower angle of 6.2° meaning the interlayer spacing expanded to 14.1 Å from 12.9 Å. Zn ion has an ionic diameter of 0.88 Å in a six-coordination, but the size of hydrated $Zn^{2+}$ with six water molecules is around 2.1 Å,[85] suggesting Zn ions are desolvated before intercalating. In the fully charged state, the peak at the lowest angle goes back to around the starting position, meaning a highly reversible reaction. The peaks around 35 ° and 62 ° present the similar tracks. Several weak peaks appear and vanish reversibly in the charging or discharging process, suggesting the reversible phases form in the reactive processes. Most of V cations reduce from 5+ to 4+ and 3+ when MnVO cathode is discharged to 0.2 V from the pristine as presented in $H_2V_3O_8$.[79] Figure 5b shows the peak at 517.0 eV corresponding to $V^{4+}$ and 515.9 eV to 3+. The characteristic peak about $V^{5+}$ can be found owing to the incomplete reaction because the delivered specific capacity of 416 mAh/g at 50 mA/g (Figure 4a) is lower than the theoretical capacity of 598 mAh/g based on the chemical valence of $V^{5+}$ fully reduces to $V^{3+}$ in the reaction. At the fully charged state, V cations are oxidized to 5+ with a small amount of 4+ as found in the pristine state. It is worth noting that the peak position of $V^{5+}$ shifts from 517.4 to 517.6 eV after the full charge (Figure 5c). In general, electron binding energy is defined as the extent of the attraction between cations and electrons through electromagnetic force in a respective atom, ion, molecule or solid, and determined by the electrostatic force of nuclei and screening effect from neighboring electrons, the formation of chemical bonds causes electron redistribution in atoms or ions and further leads to a change on binding energy.[86] The binding energy of $V^{5+}$ shifts to a higher energy state, on one hand, can be attributed to the amount of $V^{4+}$ from 18.9% to 10.4% calculated by the area ratio in the simulated XPS results. The amount of $V^{4+}$ decreases and results in a weaker attraction from the nuclei of $V^{4+}$ to the electrons in $V^{5+}$ as observed in hydrogenated $V_2O_5$.[87] The amount of $V^{4+}$ decrease also explains the capacity increase in the first two cycles as observed in Figure 4a. The trapped $Zn^{2+}$ (Figure 5d) is another possible reason because it impairs the electron-withdrawing effect of oxygen from the V cation, the reduced ionic diameter in $V^{5+}$ in comparison with that of $V^{4+}$ means the nucleus has an enhanced interaction on the electrons. The charging specific capacity is higher than the discharging one, which indicates the lower valence V cations are oxidized to 5+ in the first cycle (Figure 4a) as observed in Figure 5c. A part of the detected $Zn^{2+}$ in the fully charged state may also come from the surface adsorbed or lattice trapped $Zn^{2+}$.[79, 88] Mn (II) was detected by XPS in both fully discharged and charged states (Figure S9), meaning Mn (II) stays intact in the host crystal. Besides, the oxidation of Mn (II) would occur only at voltages above 1.62 V,[89] thus Mn (II) would not participate redox reactions in the working voltages of MnVO. EDS mapping in Figure 5e-f shows the element signals at fully discharged and charged states, Zn presents a strong and weak signal after discharging and charging in MnVO cathode, and the reversible stripping/plating reaction simultaneously proceeds on Zn metal anode as observed by SEM (Figure S10), which means Zn-ion intercalation/de-intercalation reversibly happened in the electrochemical processes. The detected Mn in both states implies it stays stable as a pillar in the crystal lattice. The recovered phases and chemical valence of constituent elements in the electrochemical processes demonstrate a reversible intercalation reaction for MnVO with the redox pairs from the V cations.

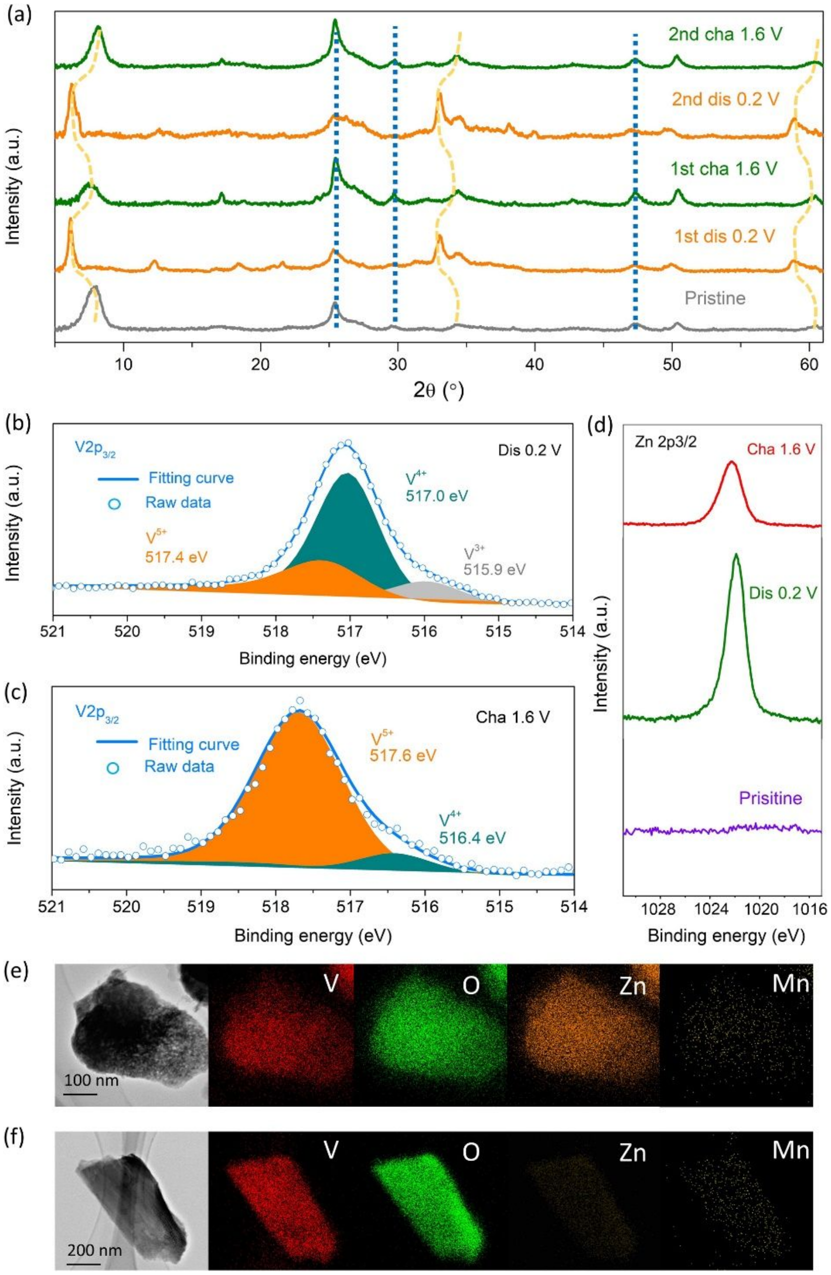

Figure 5. (a) *Ex-situ* XRD patterns of MnVO at fully discharged and charged states in the initial cycles. The shifts and recovery of the characteristic peaks suggest a reversible intercalation reaction occurring in the electrochemical processes. XPS spectra of V2p$_{3/2}$ at the fully discharged (b) and charged (c) states. The appearance of V$^{4+}$ and V$^{3+}$ agrees with the reducing reaction in the discharge process. V$^{5+}$ dominated compositions at the fully charged state mean the recovery of MnVO and a slight shift of V$^{5+}$ originates from the change of local chemical surroundings. (d) The evolution of Zn 2p$_{3/2}$ spectra in the first cycle. The remaining Zn$^{2+}$ at the fully charged state is attributed to a slight trapped Zn$^{2+}$ in the host lattice and surface adsorption even if the disassembled electrode was washed by water several times. TEM images and the corresponding EDS mapping at (e) fully discharged state and (f) fully charged state. Mn was detected at both states, suggesting Mn is stable in the crystal lattice. A slight amount of Zn ions detected at the fully charged state agrees with results from the XPS spectrum.

To discern the reasons of the disparity on the electrochemical performance of both samples, GITT plots were collected at a current density of 50 mA/g as shown in Figure 6a. The relaxation rest after charging and discharging causes the zigzag voltage profiles and the voltage recovery is used to evaluate the ion diffusion and the IR drop can be transform to internal reactive resistance (RR).[90, 91] The RRs are calculated using IR drop with the applied current density and the resistances at different steps are show in Figure 6b. For MnVO, the RRs are lower than 0.3 Ω·g in the whole process, even though a resistance bump appears around 1.0 V in the charging process. However, the RRs of VOH present an increase at the charging process and reach the maximum of 0.9 Ω·g around 1.0 V and then go down. In the discharging process, the RRs of MnVO maintain stable, but two concaves appear at 0.5 and 1.0 V in VOH. It is interesting that the positions of the bumps or concaves are identical to the redox peaks observed in CVs (Figure 3b), implying a radical difference on charge transfer in both samples. From the point of crystal structures, charge transfer in VOH prefers along the *ab* plane owing to the $[VO_n]$ polyhedra connecting to each other through edge- or point-sharing, but no points or edge contact between the interlayers along the *c*-axis.[56] In MnVO, Mn (II) ions reside into and connect [VO] interlayers so that the charge transfer is 3-dimensional and the charges from redox reaction can be transferred easily. EIS spectra (Figure 6c) compare the impedances of batteries before cycle and at the fully charged states and Table 2 lists their charge transfer resistances (CTRs). EIS spectra consist of semi-circle at high-frequency region corresponding to charge transfer resistance and a linear tail at low-frequency relating to ion diffusion.[81] MnVO presents a CTR of 63 Ω at the initial state and the CTR decreases to 24 Ω after 3 cycles, while CTRs of VOH are 177 and 38 Ω before and after cycling. The decrease of CRTs after cycling might be attributed to the activation of materials and a small amount of trapped $Zn^{2+}$ connected the $[VO_n]$ interlayers to provide more charge transfer pathways. The relationship between low-frequencies and real part of impedance (Figure 6d) can be used to calculate the Zn-ion diffusion coefficients[92] (details shown in SI) and MnVO has a higher $D_{Zn2+}$ of $3.22\times10^{-12}$ than that of $1.46\times10^{-12}$ $cm^2/s$ in VOH after the material activation. The lower RRs and CRTs and higher $D_{Zn2+}$ in MnVO guarantee the fast redox reaction and stable crystal structure supported by pillar

Mn (II) endows the excellent cycling stability at high current density of 4 A/g as shown in Figure 4b.

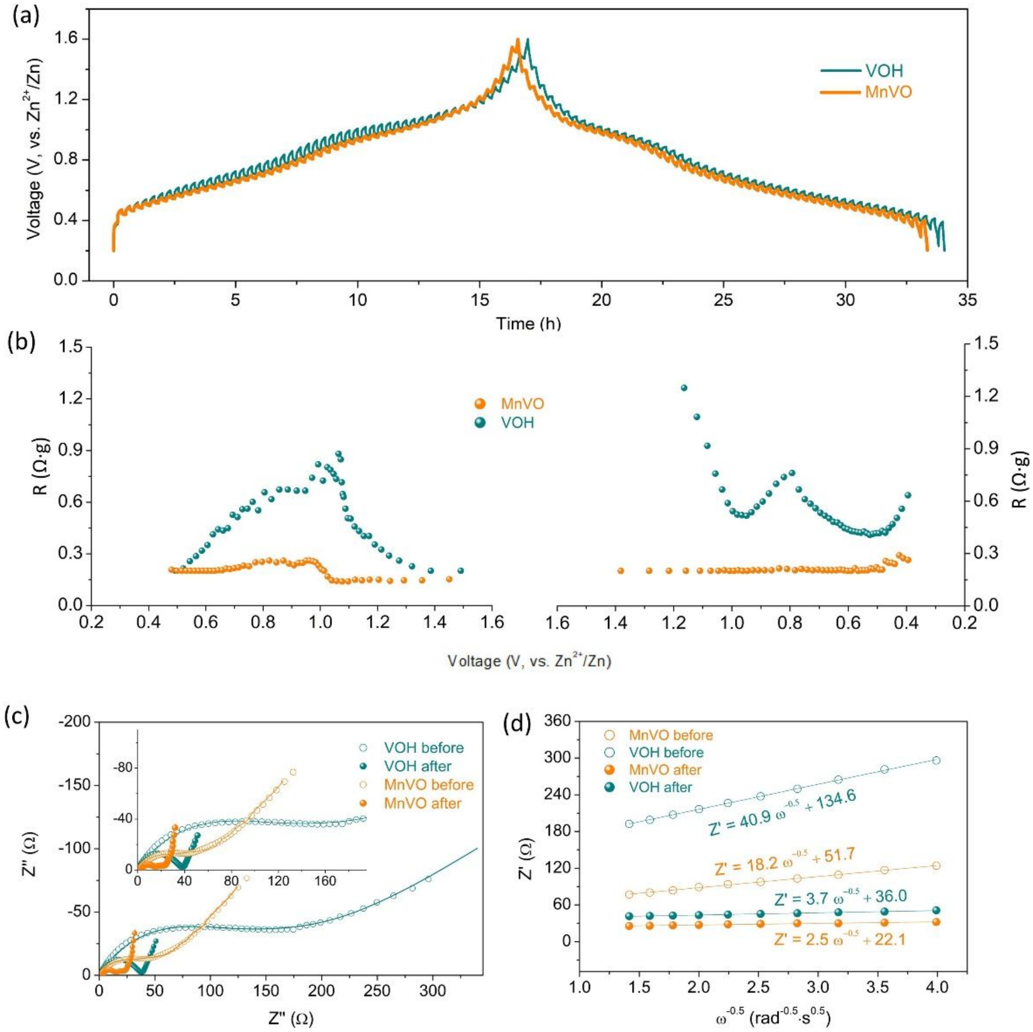

Figure 6. (a) GIIT plot collected at a current density of 50 mAh/g. (b) The reactive resistances during the charging and discharging process, the smaller resistances in MnVO suggest a better charge transfer in the redox reaction. (c) EIS spectra of both samples with the simulation curves before and after first 3 cycles with a small current density as GITT used. (d) The relationship between real part of impedance and low frequencies, the smaller slopes of the linear tendency mean the faster ion diffusion in the electrochemical processes.

Table 2. The charge transfer resistances and ion diffusion coefficients from the EIS tests

| **Samples ID** | **Label** | $R_{ct}$ **(Ω)** | $D_{Zn2+}$ **(cm²/s)** |
|---|---|---|---|
| VOH | Before cycling | 177 | $1.20\times10^{-14}$ |
| | After 3 cycles | 38 | $1.46\times10^{-12}$ |
| MnVO | Before cycling | 63 | $6.07\times10^{-14}$ |
| | After 3 cycles | 24 | $3.22\times10^{-12}$ |

Mn (II) expanded VOH achieves the structural stability and reduces reactive polarization during the repeated charge/discharge process, nickel and cobalt sulfates were also used as the raw materials to replace manganese sulfate in the synthesis processes to obtain the stabilized samples. The resulting powders exhibit similar XRD patterns as shown in Figure 7a, suggesting three samples have the similar crystal structures with MnVO as characterized and analysis above. The comparison on rate capability and cycling stability are shown in Figures 7b-c. Ni (II) vanadate (NiVO) and Co (II) vanadate (CoVO) deliver enhanced rate capability and display the excellent cycling stability at 4 A/g and high capacity retentions of 92% and 95%, respectively. Those are higher than 65% of VOH or ~ 80 of $Zn_{0.25}V_2O_5 \cdot nH_2O$ [36] or ~90% of $Na_2V_6O_{16} \cdot 1.63H_2O$[92] in the reported, demonstrating the TMCs introduction can effectively improve the Zn-ion storage performance in hydrated vanadates. The disparities on electrochemical performances of different TMCs vanadates might be attributed to the ionic size of TMCs and their electronic structures will be studied in-depth in the following work. Consequently, TMCs introduction in hydrated vanadates is a general and effective strategy to improve the electrochemical performances for various multivalent ions storage.

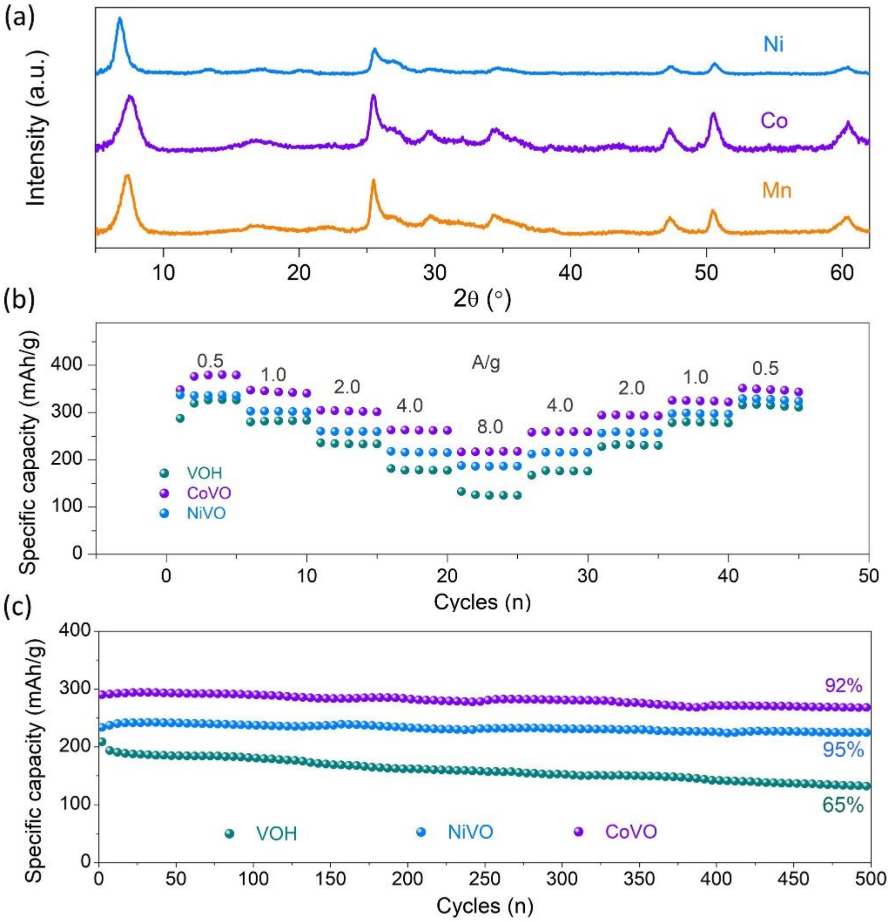

Figure 7. (a) XRD patterns of NiVO, CoVO and the reference of MnVO. The similar diffractive patterns suggest the Ni (II) and Co (II) contained samples have the same structure as MnVO. (b) Rate capability and (c) cycling stability tested at 4 A/g. Divalent transition metal cations play the same role in stabilizing the crystal structures and enhancing the cycling stability at fast charge/discharge process.

## Conclusions

Expanding the interplanar spacing of hydrated vanadate by introduction of Mn (II) ions makes the cathode more thermally and structurally stable. Chemically inserted Mn (II) ions connect [VO$_n$] layers by chemical bonds, work as pillars making the robust structure, and induce the formation of $V^{4+}$ ions resulting in expanded lattice spacing, which facilitates fast ion diffusion ($3.22\times10^{-12}$ $cm^2/s$) and enhances the electrical conductivity. MnVO cathode possesses a large storage capacity (260 mAh/g) at a higher discharge current density (4 A/g) than that of VOH. MnVO also demonstrates a capacity retention of 96% over 2,000 cycles at 4 A/g compared to 65% of VOH over 500 cycles. Chemically inserted Mn (II) ions improved reversibility by reducing the voltage polarization, resulting in an energy efficiency of 70 % in MnVO cathode battery, much higher than 40% for VOH at 4 A/g and with an open circuit voltage of MnVO battery retained at 1.36 V (85% of the cutoff voltage) after 50 days on the shelf. Divalent transition metal cations, such as Co and Ni, exhibit the same structures and stable cycling performance, suggesting that expanded VOH by introduction of TMCs is an effective and universal approach to improve or design high-performance cathode materials for aqueous Zn-ion and other multivalent ions batteries.

## Acknowledgements

This work was supported by the National Science Foundation (CBET-1803256). Part of this work was conducted at the Molecular Analysis Facility, a National Nanotechnology Coordinated Infrastructure site at the University of Washington which is supported in part by the National Science Foundation (grant NNCI-1542101), the University of Washington, the Molecular Engineering & Sciences Institute, and the Clean Energy Institute. The first author appreciates Mr. Yong Chen and Mr. Jun Qin from Neware Battery Testing Instruments for providing their technical support. MY and JY acknowledge the support from The Clean Energy Institute (CEI) at the University of Washington and the Inamori Foundation.

## References

1. M. Li, J. Lu, Z. Chen and K. Amine, *Adv. Mater.*, 2018, **30**, 1800561.
2. A. Manthiram, J. C. Knight, S.T. Myung, S.M. Oh and Y.K. Sun, *Adv. Energy Mater.*, 2016, **6**, 1501010.
3. M. H. Han, E. Gonzalo, G. Singh and T. Rojo, *Energy Environ. Sci.*, 2015, **8**, 81-102.
4. M. S. Whittingham, *Science*, 1976, **192**, 1126-1127.
5. M. S. Whittingham, *J. Solid State Chem.*, 1979, **29**, 303-310.
6. M. Armand and J. M. Tarascon, *Nature*, 2008, **451**, 652-657.
7. X.Y. Lang, B.T. Liu, X.M. Shi, Y.Q. Li, Z. Wen and Q. Jiang, *Adv. Sci.*, 2016, **3**, 1500319.
8. A. Yoshino, *Angew. Chem. Int. Edit*, 2012, **51**, 5798-5800.
9. N. A. Godshall, I. D. Raistrick and R. A. Huggins, *Mater. Res. Bull.*, 1980, **15**, 561-570.
10. K. Mizushima, P. C. Jones, P. J. Wiseman and J. B. Goodenough, *Mater. Res. Bull.*, 1980, **15**, 783-789.
11. R. C. Massé, C. Liu, Y. Li, L. Mai and G. Cao, *Nat. Sci. Rev.*, 2017, **4**, 26-53.
12. X. Liu, D. Ren, H. Hsu, X. Feng, G.L. Xu, M. Zhuang, H. Gao, L. Lu, X. Han, Z. Chu, J. Li, X. He, K. Amine and M. Ouyang, *Joule*, 2018, **2**, 2047-2064.
13. L. Suo, O. Borodin, T. Gao, M. Olguin, J. Ho, X. Fan, C. Luo, C. Wang and K. Xu, *Science*, 2015, **350**, 938-943.

14. Y. Yamada, K. Usui, K. Sodeyama, S. Ko, Y. Tateyama and A. Yamada, *Nat. Energy*, 2016, **1**, 16129.
15. P. Canepa, G. Sai Gautam, D. C. Hannah, R. Malik, M. Liu, K. G. Gallagher, K. A. Persson and G. Ceder, *Chem. Rev.*, 2017, **117**, 4287-4341.
16. M. Song, H. Tan, D. Chao and H. J. Fan, *Adv. Funct. Mater.*, 2018, **28**, 1802564.
17. R. J. Gummow, G. Vamvounis, M. B. Kannan and Y. He, *Adv. Mater.*, 2018, **30**, 1801702.
18. J. Muldoon, C. B. Bucur and T. Gregory, *Chem. Rev.*, 2014, **114**, 11683-11720.
19. G. Fang, J. Zhou, A. Pan and S. Liang, *ACS Energy Lett.*, 2018, **3**, 2480-2501.
20. Y. Li, J. Fu, C. Zhong, T. Wu, Z. Chen, W. Hu, K. Amine and J. Lu, *Adv. Energy Mater.*, 2019, **9**, 1802605.
21. A. Konarov, N. Voronina, J. H. Jo, Z. Bakenov, Y.K. Sun and S.T. Myung, *ACS Energy Lett.*, 2018, **3**, 2620-2640.
22. G. G. Yadav, J. W. Gallaway, D. E. Turney, M. Nyce, J. Huang, X. Wei and S. Banerjee, *Nat. Commun.*, 2017, **8**, 14424.
23. L. Wang, X. Cao, L. Xu, J. Chen and J. Zheng, *ACS Sustain. Chem. Eng.*, 2018, **6**, 16055-16063.
24. S. Zhao, B. Han, D. Zhang, Q. Huang, L. Xiao, L. Chen, D. G. Ivey, Y. Deng and W. Wei, *J. Mater. Chem.A*, 2018, **6**, 5733-5739.
25. B. Lee, H. R. Lee, H. Kim, K. Y. Chung, B. W. Cho and S. H. Oh, *Chem. Commun.*, 2015, **51**, 9265-9268.
26. M. Chamoun, W. R. Brant, C.W. Tai, G. Karlsson and D. Noréus, *Energy Storage Mater.*, 2018, **15**, 351-360.
27. H. Pan, Y. Shao, P. Yan, Y. Cheng, K. S. Han, Z. Nie, C. Wang, J. Yang, X. Li, P. Bhattacharya, K. T. Mueller and J. Liu, *Nat. Energy*, 2016, **1**, 16039.
28. N. Zhang, F. Cheng, J. Liu, L. Wang, X. Long, X. Liu, F. Li and J. Chen, *Nat. Commun.*, 2017, **8**, 405.
29. P. Hu, M. Yan, T. Zhu, X. Wang, X. Wei, J. Li, L. Zhou, Z. Li, L. Chen and L. Mai, *ACS Appl. Mater. Interfaces.*, 2017, **9**, 42717-42722.
30. N. Zhang, Y. Dong, M. Jia, X. Bian, Y. Wang, M. Qiu, J. Xu, Y. Liu, L. Jiao and F. Cheng, *ACS Energy Lett.*, 2018, **3**, 1366-1372.
31. P. Senguttuvan, S.D. Han, S. Kim, A. L. Lipson, S. Tepavcevic, T. T. Fister, I. D. Bloom, A. K. Burrell and C. S. Johnson, *Adv. Energy Mater.*, 2016, **6**, 1600826.
32. J. Ding, Z. Du, L. Gu, B. Li, L. Wang, S. Wang, Y. Gong and S. Yang, *Adv. Mater.*, 2018, **30**, 1800762.
33. B. Sambandam, V. Soundharrajan, S. Kim, M. H. Alfaruqi, J. Jo, S. Kim, V. Mathew, Y.K. Sun and J. Kim, *J. Mater. Chem.A*, 2018, **6**, 3850-3856.
34. V. Soundharrajan, B. Sambandam, S. Kim, M. H. Alfaruqi, D. Y. Putro, J. Jo, S. Kim, V. Mathew, Y.K. Sun and J. Kim, *Nano Lett.*, 2018, **18**, 2402-2410.
35. B. Tang, G. Fang, J. Zhou, L. Wang, Y. Lei, C. Wang, T. Lin, Y. Tang and S. Liang, *Nano Energy*, 2018, **51**, 579-587.
36. D. Kundu, B. D. Adams, V. Duffort, S. H. Vajargah and L. F. Nazar, *Nat. Energy*, 2016, **1**, 16119.
37. Z. Liu, G. Pulletikurthi and F. Endres, *ACS Appl. Mater. Interfaces*, 2016, **8**, 12158-12164.

38. R. Trócoli and F. La Mantia, *Chemsuschem*, 2015, **8**, 481-485.
39. G. Kasiri, R. Trócoli, A. Bani Hashemi and F. La Mantia, *Electrochim. Acta*, 2016, **222**, 74-83.
40. L. Zhang, L. Chen, X. Zhou and Z. Liu, *Sci. Rep.*, 2015, **5**, 18263.
41. Y. Cheng, L. Luo, L. Zhong, J. Chen, B. Li, W. Wang, S. X. Mao, C. Wang, V. L. Sprenkle, G. Li and J. Liu, *ACS Appl. Mater. Interfaces*, 2016, **8**, 13673-13677.
42. M. S. Chae, J. W. Heo, S.C. Lim and S.T. Hong, *Inorg. Chem.*, 2016, **55**, 3294-3301.
43. W. Liu, J. Hao, C. Xu, J. Mou, L. Dong, F. Jiang, Z. Kang, J. Wu, B. Jiang and F. Kang, *Chem. Commun.*, 2017, **53**, 6872-6874.
44. H. Li, Q. Yang, F. Mo, G. Liang, Z. Liu, Z. Tang, L. Ma, J. Liu, Z. Shi and C. Zhi, *Energy Storage Mater.*, 2018, DOI: https://doi.org/10.1016/j.ensm.2018.10.005.
45. Q. Zhao, W. Huang, Z. Luo, L. Liu, Y. Lu, Y. Li, L. Li, J. Hu, H. Ma and J. Chen, *Sci. Adv.*, 2018, **4**, eaao1761.
46. D. Kundu, P. Oberholzer, C. Glaros, A. Bouzid, E. Tervoort, A. Pasquarello and M. Niederberger, *Chem. Mater.*, 2018, **30**, 3874-3881.
47. G. Fang, C. Zhu, M. Chen, J. Zhou, B. Tang, X. Cao, X. Zheng, A. Pan and S. Liang, *Adv. Funct. Mater.*, 2019, **29**, 1808375.
48. T. Gupta, A. Kim, S. Phadke, S. Biswas, T. Luong, B. J. Hertzberg, M. Chamoun, K. Evans-Lutterodt and D. A. Steingart, *J.Power Sources*, 2016, **305**, 22-29.
49. W. Xu, C. Sun, K. Zhao, X. Cheng, S. Rawal, Y. Xu and Y. Wang, *Energy Storage Mater.*, 2019, **16**, 527-534.
50. https://en.wikipedia.org/wiki/Abundance_of_elements_in_Earth%27s_crust.
51. M. Yan, P. He, Y. Chen, S. Wang, Q. Wei, K. Zhao, X. Xu, Q. An, Y. Shuang, Y. Shao, K. T. Mueller, L. Mai, J. Liu and J. Yang, *Adv. Mater.*, 2018, **30**, 1703725.
52. F. Ming, H. Liang, Y. Lei, S. Kandambeth, M. Eddaoudi and H. N. Alshareef, *ACS Energy Lett.*, 2018, **3**, 2602-2609.
53. Y. Yang, Y. Tang, G. Fang, L. Shan, J. Guo, W. Zhang, C. Wang, L. Wang, J. Zhou and S. Liang, *Energy Environ. Sci.*, 2018, **11**, 3157-3162
54. C. Xia, J. Guo, P. Li, X. Zhang and H. N. Alshareef, *Angew. Chem. Int. Edit*, 2018, **57**, 3943-3948.
55. C. C. Torardi, C. R. Miao, M. E. Lewittes and Z. Li, *J. Solid State Chem.*, 2002, **163**, 93-99.
56. J. Yao, Y. Li, R. C. Massé, E. Uchaker and G. Cao, *Energy Storage Mater.*, 2018, **11**, 205-259.
57. C. O'Dwyer, V. Lavayen, S. B. Newcomb, M. A. Santa Ana, E. Benavente, G. González and C. M. Sotomayor Torres, *J. Electrochem. Soc.*, 2007, **154**, K29-K35.
58. Q. Wei, J. Liu, W. Feng, J. Sheng, X. Tian, L. He, Q. An and L. Mai, *J. Mater. Chem.A*, 2015, **3**, 8070-8075.
59. D. McNulty, D. N. Buckley and C. O'Dwyer, *RSC Adv*, 2016, **6**, 40932-40944.
60. C. L. Londoño-Calderón, C. Vargas-Hernández and J. F. Jurado, *Revista mexicana de física*, 2010, **56**, 411-415.
61. S. Boukhalfa, K. Evanoff and G. Yushin, *Energy Environ. Sci.*, 2012, **5**, 6872-6879.
62. C. Sanchez, J. Livage and G. Lucazeau, *J. Raman Spectrosc.*, 1982, **12**, 68-72.
63. J. Lee, S. Badie, P. Srimuk, A. Ridder, H. Shim, S. Choudhury, Y.C. Nah and V. Presser, *Sustain. Energy & Fuels*, 2018, **2**, 577-588.

64. S. V. Burdyukh, O. Y. Berezina, A. L. Pergament, L. A. Lugovskaya and Y. G. Kolyagin, *Thin Solid Films*, 2018, **656**, 22-29.
65. P. Remith and N. Kalaiselvi, *Nanoscale*, 2014, **6**, 14724-14732.
66. X. Li, C. Liu, C. Zhang, H. Fu, X. Nan, W. Ma, Z. Li, K. Wang, H. Wu and G. Cao, *ACS Appl. Mater. Interfaces*, 2016, **8**, 24629-24637.
67. S. Zhang, M. Hou, L. Hou and W. Ma, Manganese and vanadium nanomaterial synthesis, application, *China Pat.*, 2015.
68. W. M. Haynes, *CRC Handbook of Chemistry and Physics, 93rd Edition*, Taylor & Francis, 2012.
69. F. Liu, Z. Chen, G. Fang, Z. Wang, Y. Cai, B. Tang, J. Zhou and S. Liang, *Nano-Micro Lett.*, 2019, **11**, 25.
70. C. Li, P. Zheng, J. Li, H. Zhang, Y. Cui, Q. Shao, X. Ji, J. Zhang, P. Zhao and Y. Xu, *Angew. Chem. Int. Edit*, 2003, **42**, 5063-5066.
71. H. Song, C. Liu, C. Zhang and G. Cao, *Nano Energy*, 2016, **22**, 1-10.
72. Y. Liu, M. Clark, Q. Zhang, D. Yu, D. Liu, J. Liu and G. Cao, *Adv. Energy Mater.*, 2011, **1**, 194-202.
73. Y. Wang, J. Li and Z. Wei, *J. Mater. Chem.A*, 2018, **6**, 8194-8209.
74. L. Chen, Y. Ruan, G. Zhang, Q. Wei, Y. Jiang, T. Xiong, P. He, W. Yang, M. Yan, Q. An and L. Mai, *Chem. Mater.*, 2019, DOI: 10.1021/acs.chemmater.8b03409.
75. X. Dai, F. Wan, L. Zhang, H. Cao and Z. Niu, *Energy Storage Mater.*, 2018, **17**, 143-150.
76. J. Wang, J. Polleux, J. Lim and B. Dunn, *J. Phys. Chem. C*, 2007, **111**, 14925-14931.
77. V. Augustyn, J. Come, M. A. Lowe, J. W. Kim, P.L. Taberna, S. H. Tolbert, H. D. Abruña, P. Simon and B. Dunn, *Nat. Mater.*, 2013, **12**, 518-522.
78. B.T. Liu, X.M. Shi, X.Y. Lang, L. Gu, Z. Wen, M. Zhao and Q. Jiang, *Nat. Commun.*, 2018, **9**, 1375.
79. Q. Pang, C. Sun, Y. Yu, K. Zhao, Z. Zhang, M. Voyles Paul, G. Chen, Y. Wei and X. Wang, *Adv. Energy Mater.*, 2018, **8**, 1800144.
80. M. H. Alfaruqi, V. Mathew, J. Song, S. Kim, S. Islam, D. T. Pham, J. Jo, S. Kim, J. P. Baboo, Z. Xiu, K.S. Lee, Y.K. Sun and J. Kim, *Chem. Mater.*, 2017, **29**, 1684-1694.
81. F. Wang, E. Hu, W. Sun, T. Gao, X. Ji, X. Fan, F. Han, X.Q. Yang, K. Xu and C. Wang, *Energy Environ. Sci.*, 2018, **11**, 3168-3175.
82. C. Liu, S. Wang, C. Zhang, H. Fu, X. Nan, Y. Yang and G. Cao, *Energy Storage Mater.*, 2016, **5**, 93-102.
83. S.H. Chung and A. Manthiram, *ACS Energy Lett.*, 2017, **2**, 1056-1061.
84. F. Beguin and E. Frackowiak, *Supercapacitors: Materials, Systems and Applications*, Wiley-VCH, 2013.
85. Y. Marcus, *Chem. Rev.*, 1988, **88**, 1475-1498.
86. P. v. d. Heide, *X-Ray Photoelectron Spectroscopy: An Introduction to Principles and Practices*, John Wiley & Sons, Inc., 2011.
87. X. Peng, X. Zhang, L. Wang, L. Hu, S. H.S. Cheng, C. Huang, B. Gao, F. Ma, K. Huo and P. K. Chu, *Adv. Funct. Mater.*, 2016, **26**, 784-791.
88. T. Wei, Q. Li, G. Yang and C. Wang, *J. Mater. Chem.A*, 2018, **6**, 20402-20410.
89. C. Zhu, G. Fang, J. Zhou, J. Guo, Z. Wang, C. Wang, J. Li, Y. Tang and S. Liang, *J. Mater. Chem.A*, 2018, **6**, 9677-9683.

90. Y. J. Zhu and C. S. Wang, *J. Phys. Chem. C*, 2010, **114**, 2830-2841.
91. D. W. Dees, S. Kawauchi, D. P. Abraham and J. Prakash, *J.Power Sources*, 2009, **189**, 263-268.
92. P. Hu, T. Zhu, X. Wang, X. Wei, M. Yan, J. Li, W. Luo, W. Yang, W. Zhang, L. Zhou, Z. Zhou and L. Mai, *Nano Lett.*, 2018, **18**, 1758-1763.

## Broader context

Aqueous zinc ion batteries with nonflammable electrolyte offer high safety, fast charge/discharge capability, long-term cycling stability, and low cost with comparable energy density to lithium ion batteries. However, the lack of cathodes with high practical capacity, high discharge voltage, low self-discharge, and cycling stability remains an imperative challenge. Hydrated vanadium pentoxide (VOH) delivers a specific capacity as high as 400 mAh/g but suffers from structural degradation because of the weak Van de Waals force between the layers. In the present work, divalent transition metal cations (TMs) were chemically pre-inserted to VOH, resulting in much larger storage capacity and higher discharge voltage, and enhanced rate capability and cycling stability in comparison with VOH owing collectively to enlarged interplanar spacing, stabilized crystal structure, catalytic effect, and improved charge and ion transport properties. The increased energy efficiency and reduced voltage degradation reveal a great potentiality for commercial applications.